

# Analysis of 3D Computed Tomographic Imaging of Ground-wall Insulation for AC Rotating Machines

A. Contin, M. Piller and G. Schena

D.I.A. University of Trieste  
Via A. Valerio 10  
Trieste, 34127 Italy

## ABSTRACT

The X-ray Computed Tomography (X-CT) has been used to reconstruct the internal features of two types of ground-wall insulation for ac rotating machines. Four samples whose insulation was designed for a rated voltage of 11 kV, were extracted from different coils and scanned using X-CT. The 3D virtual volumes have been visually inspected stacking the tomographic slices to identify the internal morphological features that is, the different materials in the inner structure, the presence of minute voids, gas bubbles, anomalous densities, wrinkled or damaged tape layers. The tomographic volumes have been segmented into different gray-levels resorting to luminosity histograms with the purpose to differentiate the structural materials and extract only specific anomalies. In particular, the binary segmentation has been adopted to investigate the distributions of the void enclosures. The use of X-CT to investigate the internal structure of complex insulation systems, opens significant perspectives in improving the insulation manufacturing quality.

Index Terms - Rotating machines, ground-wall insulation, X-ray tomography, vacuum pressure impregnation, VPI process.

## 1 INTRODUCTION

**GROUND-WALL** insulation systems for Vacuum Pressure Impregnation (VPI) stator windings of ac rotating machines can be realized using different types of mica/fiber-glass tapes. Polymeric films are also used to form four-layer tapes. Mica is adopted to withstand the partial discharge activity and the electrical-tree growth while the fiber glass provides mechanical strength and flexibility to the tape. Depending on the voltage rate, a number of half-superimposed tape-layers is realized under controlled tension either manually or most often using taping machines. Mica-based tapes are also adopted to form the turn or strand insulation. Both coils or complete stators are impregnated with resins in a VPI controlled environment to fill all the voids and obtain a compact insulation. Despite the vacuum and pressure, some small voids remain embedded within the ground-wall, [1, 2]. These are in form of small gas bubbles in the resin or elongated slim voids well-adjusted with the texture of the taping. Gas inclusions have lower breakdown strength than the solid materials. In the presence of electric field above the partial discharge inception values, voids can become discharge sites, [2]. Thus, the characterization of the critical regions of the ground-wall insulation such as voids,

cracks, delaminations, resin accumulations at the tape overlaps, wrinkled or disrupted mica-layers and solid inclusions that facilitate the propagation of electrical trees that can reduce the insulation lifetime, [3], is of great interest. These defect typologies have already been evidenced mainly by planar micrographs (see e.g., [4, 5]) but their representation in three dimensions (3D) is quite attractive.

A realistic 3D virtual volume of the insulation interiors can be obtained using the X-Ray Computed Tomography (X-CT). X-CT does not require any prior treatment of the samples and leaves intact the 3D inner structure of the object under test, [6, 7]. Industrial applications of X-CT are increasing rapidly as a tool for non destructive evaluation of the morphology of composite materials, quality control, dimensional and tolerance verification of complex objects, [8]. Thus, the use of X-CT to explore the internal features of the ground-wall insulation with the aim to evaluate the penetration of the impregnation resin and the taping characteristics or the possible anomalies, appears quite promising to improve the insulation quality. Moreover, the availability of 3D virtual image of the insulation allows to simulate the electric field distribution and in particular, its distortion due to the presence of the internal defects, [10].

Among the different types of tomographic systems, micro X-CT provides high-penetration capability and good spatial resolution required to investigate particularly resin

penetration within the composite insulation, [9, 11, 12]. Resolution of few microns can be achieved with object sizes of few cm<sup>3</sup>. Composite materials present different X-ray attenuation when they pass through different materials. The right set-up of the scanning system has to be selected to capture the smallest structures of the composite material also with minor differences in density of the impregnation resin.

In this investigation, samples belonging to two different ground-wall insulation systems (two and four layer mica-tapes provided by different fiber-glass texture), having sizes of about 0.25 cm<sup>3</sup>, were gently removed from complete coils and scanned using X-CT system based on a cone-beam micro-focus source. The 3D virtual volumes were reconstructed measuring the X-ray attenuation and creating 3D maps where the grey-levels are associated to the internal densities. The distribution of regions with different internal features can be visualized by means of slicing or using 3D volume rendering procedures. Histograms representing the distribution of the grey-levels (luminosity histogram) have been analyzed to segment both the voids and the high density inclusions from the solid insulation (binary segmentation). Multiple segmentation is also used to differentiate the materials and to obtain an image of the internal structure that can be adopted to simulate the electric field distribution in a volume, [10]. By this way, the volume, the shape and the density of the distributed micro-voids can be estimated and additional information on the influence of the tape characteristics on the resin penetration, can be achieved.

## 2 COIL CHARACTERISTICS AND SAMPLE PREPARATION

Two types of ground-wall insulation both designed for a rated voltage of 11 kV, have been considered in this investigation. The first insulation (Type-A) is based on four-layer tape having a thickness of about 0.15 mm. It is composed by mica-paper reinforced with thin-texture of fiber-glass completed with two layers of a polyester film. The total insulation thickness is about 2.9 mm for an electric stress of about 2.20 kV/mm. The second insulation (Type-B) is based on a two-layer tape (mica-paper tapes reinforced with large texture fiber-glass). The tape thickness is about 0.15 mm for an insulation thickness of 2.7 mm (electric stress of about 2.3 kV/mm). The different coils were realized using the same materials and the same thickness but changing the VPI parameters. Both insulations have been wounded with tapes half superimposed. In both cases, the turn insulation is realized using mica-paper tape. All the coils have been completed with slot and end-arm stress grading system and impregnated with epoxy or polyester-immide resin for Type A and Type B insulation, respectively. Figure 1 shows a cross-section of two coils. The coil-section sizes are (A) 39 mm x 16 mm and (B) 27 mm x 16 mm, respectively.

Coil portions having sizes of about 5 mm x 5 mm x 10 mm each, that include both the ground-wall insulation and part of the conductors were obtained sectioning the coils.

Dotted lines reported on a coil section of Figure 1, indicate qualitatively the insulation portions removed and scanned with X-CT. The test results discussed here are relevant to four samples named A1, A2 and B1, B2 for Type-A and Type-B insulation, respectively.

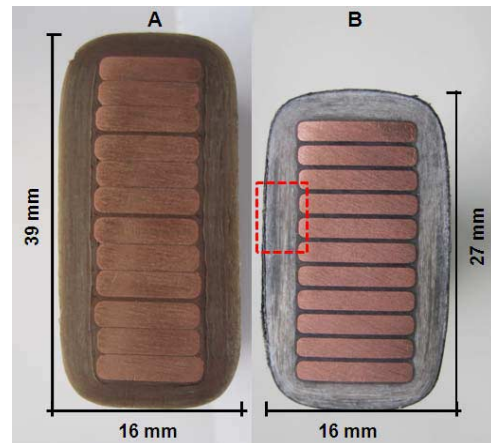


**Figure 1.** Cross sections of two coils under test. A) Type-A and B) Type-B ground-wall insulation. The dotted lines indicates qualitatively the coil portion removed and scanned with X-CT.

## 3 THE X-RAY COMPUTED TOMOGRAPHY

### 3.1 PRINCIPLES OF MICRO X-CT

In general, the X-CT set-up is composed by a X-ray source, a CCD camera or a flat panel detector and a turn-table (Figure 2). A cone-beam of X-rays generated by a micro-focus source, goes through the object and hits the screen of a CCD camera. As the X-rays pass through the object, their intensity is differently attenuated depending on the material density. Each pixel of the CCD camera ( $P_{i,j}$ ) records an intensity of the X-ray emerging from the object. The attenuation of the X-rays is given by the Beer-Lambert law, [13]:

$$\log\left(\frac{I_0}{I_{i,j}}\right) = \int_{path} \mu(E, s) ds \quad (1)$$

where  $\mu$  is the attenuation coefficient of the material along the linear path from the X-ray source to the specific pixel  $P_{i,j}$ ,  $I_0$  is the intensity of the X-ray beam the incident (upon the object),  $E$  denotes the photon energy,  $I_{i,j}$  is the intensity emerging from the object and  $s$  is the linear abscissa along the path. The source energy is selected on the basis of the sample characteristics after a preliminary calibration.

The 3D image reconstruction requires a number of radiographies obtained rotating the object under tests by small angular steps until completing the full rotation. After a step rotation, different grey levels can be recorded by the same pixel because the total attenuation of the X-rays can be modified by the different densities encountered along the new path. Considering the sketch of an opaque object having two higher density inclusions (see Figure 3), X-rays are more attenuated along the horizontal direction than the vertical one due to the different alignment of the two

inclusions. Thus, the CCD camera records different luminosity intensities when the X-rays have a horizontal or vertical alignment. Several hundreds of projections are usually acquired depending on the diameter of the object and the X-CT resolution required.

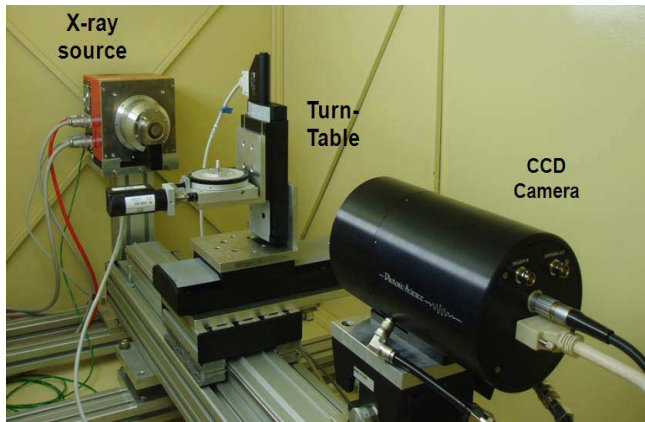


Figure 2. The X-CT set-up.

### 3.2 3D VIRTUAL VOLUME RECONSTRUCTION

The mathematical principle of the 3D virtual volume reconstruction, that is the association of a grey level to each voxel is casted around the Radon inverse transformation [13], adapted by Feldkamp for diverging cone-beams, [14]. The algorithm considers the back projection of all the digital radiographies recorded during a 360° rotation (Filtered Back Projection (FBP), [14]). The basis of the FBP algorithm referred to the example of Figure 3, are summarized in Figure 4. The gray-levels associated to the two radiographies are back projected and 4 combined gray-level values are distributed in 5 x 3 elements (Figure 4A). The data normalization provides the gray-levels associated to each voxel, (Figure 4B). By this way, an image of the inner structure of the original object is reconstructed and available for further analysis. It must be pointed out that the original resolution of the projections is invariably degraded by the interpolation that the FBP algorithm applies redistributing the pixel luminosity to all the voxels laying on the path between the focal spot and the detector pixel. For this reason the nominal resolution associated to a tomographic volume is referred to as the voxel size.

### 3.3 THE EXPERIMENTAL X-CT SET-UP

The X-CT adopted in this investigation is a custom designed station, named TOMOLAB, based on a sealed-type cone-beam Hamamatsu X-ray source having a micro-focus with a minimal spot size of 5 $\mu$ m, operating in a voltage range from 20 kV<sub>p</sub> to 130 kV<sub>p</sub> at a maximum current of 0.3 mA (see Figure 2 for the complete set-up). A 12 bit Photonic Science VHR CCD camera provides a combination of large field of view for objects having a maximum size of 50 mm x 33 mm. The CCD detector has 4008x2672 square pixels with 12.5  $\mu$ m x 12.5  $\mu$ m side. Samples are positioned on a high precision step angle turn-table located between the X-ray source and the CCD camera. The whole set-up is

enclosed in a certified cabinet that protects the operating personnel from radiation exposure. Preliminary tests indicate an operating voltage of 50 kV<sub>p</sub> as a good compromise between the needed resolution, the small density contrast of the impregnation resin and the thickness of the object undergoing scanning. In this investigation, 1400 tomographic projections which corresponds to 0.25 angular degrees, have been recorded during complete rotation of the object.

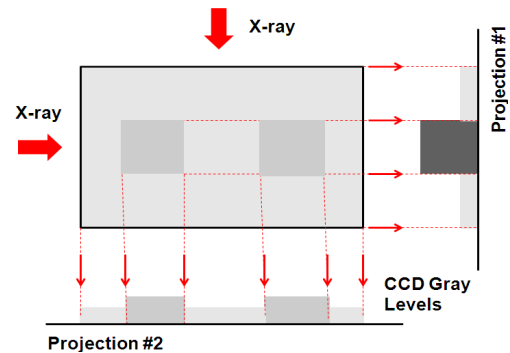


Figure 3. Sketch of the X-CT projections of an object having higher density inclusions.

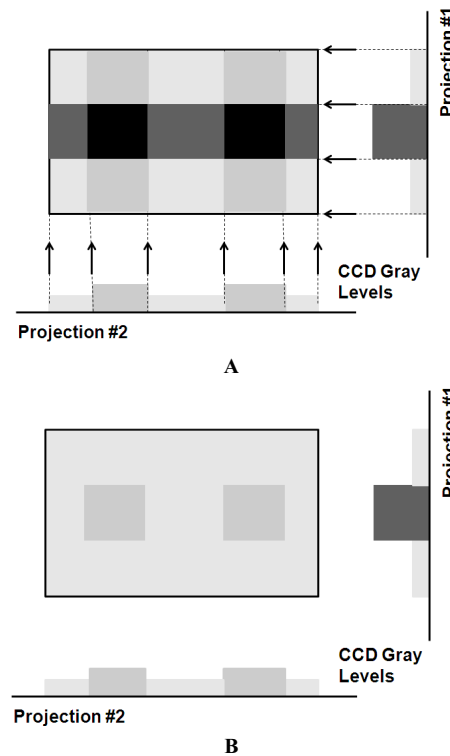


Figure 4. Sketch of the back-projection algorithm. A) the back projection of the radiographies; B) the object reconstruction after data normalization.

The TOMOLAB system provides automatically the X-CT results as a set of tomographic slices having the same resolution of the X-ray radiographies (12.5  $\mu$ m x 12.5  $\mu$ m).

After the FBP reconstruction, the gray discontinuities between adjacent voxels have been smoothed using a median filter that replace the gray level associated with a given voxel with the median value of the luminosity of the 27 neighboring voxels sorted by intensity (3 x 3 x 3 voxels that surround the

voxel under consideration). The median filter is a nonlinear, parameter free, edge preserving filter and it is widely used in image processing applications [15].

### 3.4 VISUALIZATION OF 3D DIGITAL VOLUMES

Specialized software tools provide realistic 3D images for a visual inspection. Figure 5 shows two different global views of Type-B2 and Type-A1 samples (Figure 5A and 5B, respectively). As can be seen, the layers of both the turn and the ground wall insulation, are visible in Figure 5A while a more compact structure due to the different tape characteristics, is evident in Figure 5B.

The tomographic volumes can be virtually rotated or sectioned by planes having different orientation with the aim to optimize the sample exposures. Figure 6 reports two sections of sample Type-B2 of Figure 5A. With reference of the conductors' direction, Figures 6A and 6B show an orthogonal and 45° plain section, respectively. Using the view of Figure 6A, the layers of the turn insulation are more evident. The oblique section of the same sample reported in Figure 6B allows to observe additional details of the inner structure (tape layers and large-texture fiber-glass), the tape wrinkles and larger voids (darker spots) between the two turn-insulations, details that can be examined with accuracy by slicing and enlarging the 3D images. The thinner and the larger texture of the fiber-glass adopted in Type-A and Type-B insulation, are clearly visible in Figure 7 (Figures 7A and 7B for A1 and B1 samples, respectively). Both pictures have size of 4.5 mm x 4.5 mm.

The inner structure of the ground-wall insulation can be visually explored to evaluate the resin penetration as well as to find out its anomalies such as voids, cracks, delaminations, resin accumulations at the tape overlaps, tape displacements, wrinkled or disrupted mica-layers and solid inclusions. Figure 8 shows some defects discovered during the visual inspection of Type-B2 sample. In particular, Figure 8A shows a detail of tape displacements and distributed microvoids while a high density inclusion (the white object between the tape layers) is evident in Figure 8B. A large void embedded in the impregnation resin between the turn insulation, is shown in Figure 8C. It must be point out that due to the presence of areas with a low density of the impregnation resin, it is sometime difficult to discriminate between micro voids and resin. This result can be achieved by processing the gray-levels associated to the voxels and resorting to the binary segmentation.

## 4 SEGMENTATION AND VISUALIZATION

The separation of the voids and the other density anomalies from the solid framework is typically performed analyzing the voxel luminosity histograms; it classifies all the voxels of the tomographic volume in narrow gray-scale intervals, [16]. The lower and the higher values of the luminosity correspond to lower (void) and higher density phase. A luminosity histogram relevant to Type-A2 sample is reported in Figure 9 as an example. Three different gray-level distributions that approximately correspond to void, resin and solid phase, are evident in the figure. Although the

most general case involves a two-phase system made of voids that need to be separated by the solid framework, also multi-phase separation is often required in order to distinguish different solid phases inside a composite insulation. The basic concept lies in the proper selection of threshold values on the histogram.

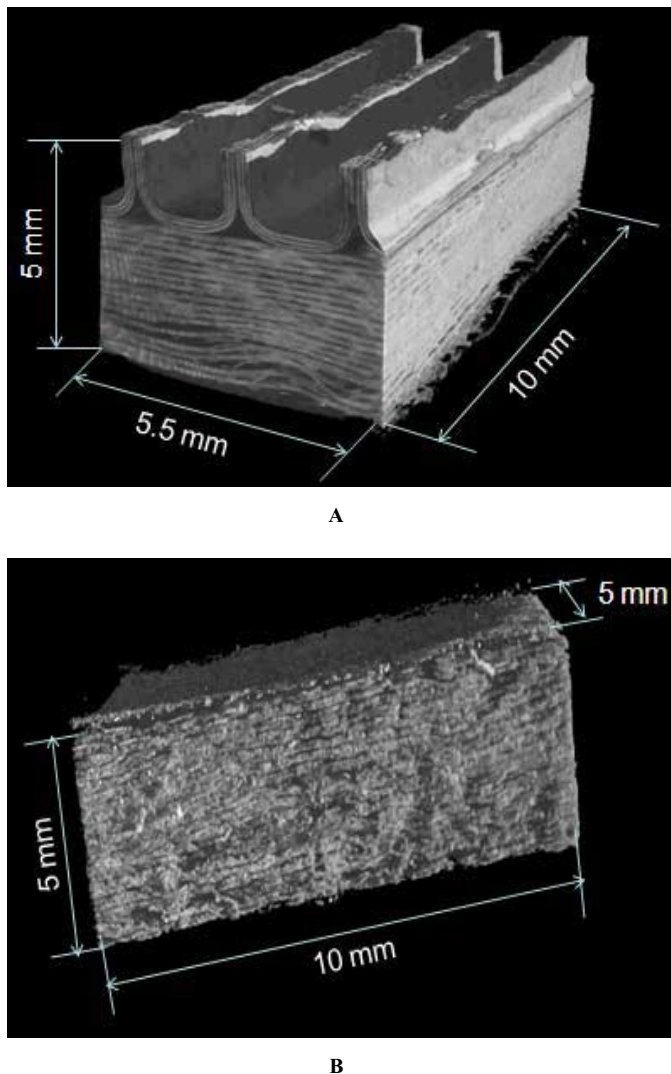


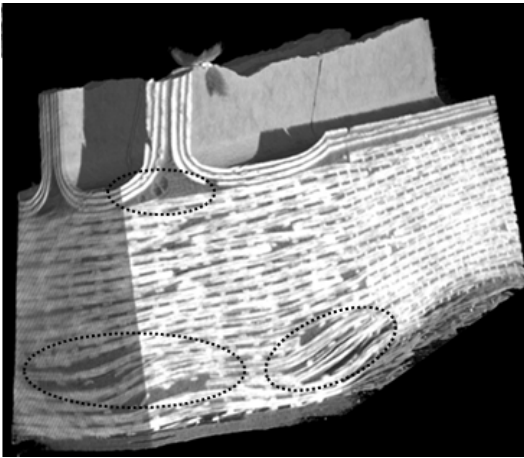
**Figure 5.** Different views of two samples: A) Type-B2 and B) Type-A1 ground-wall insulation.

### 4.1 BINARY SEGMENTATION FOR VOID PARTITION

The gray-scale 3D digital images can be transformed in 3D binary images containing only zeros and ones useful to represent e.g., the void distribution within the solid, [16]. This transformation is known as binary segmentation and refers to the determination of the phase type of each voxel. Black and white colors are assigned to the voxels where the gray-scale values result lower or higher than a selected threshold level. Preliminary tests were performed to select empirically the most suitable threshold on the luminosity histogram. The impregnation resin does not fill completely all the spaces with the same density thus, a distribution of gray-levels is associated to the transition from higher to lower density resin.

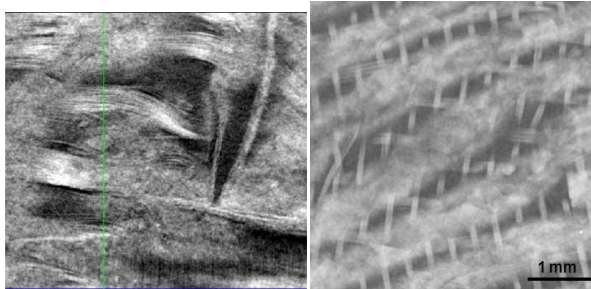


A



B

**Figure 6.** Different sections of the Type-B2 sample of Figure 5A: A) orthogonal section and B) 45° section with respect the conductor' direction.



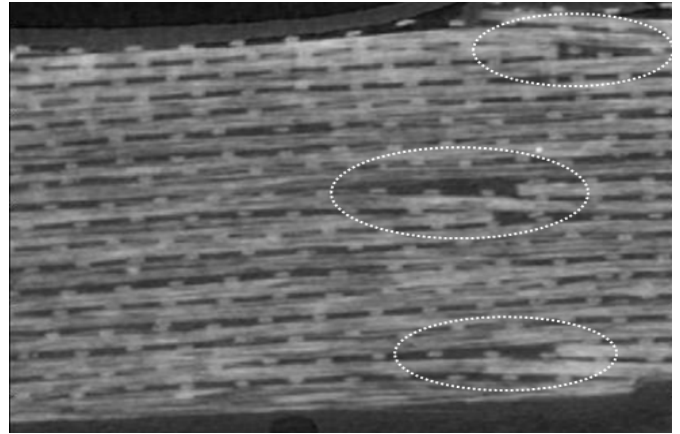
A

B

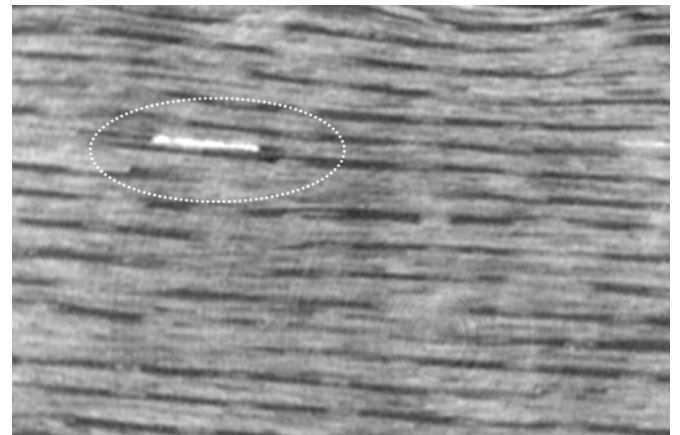
**Figure 7.** Details of the fiber-glass texture (7.5 mm x 7.5 mm): A) Type-A1 thin texture; B) Type-B1 large texture.

The same holds for the void phase (from the real void to very low-density resin). If the gray-level distributions relevant to the void and resin phases are partially overlapped, the most reasonable threshold has to be selected close to the intersection of the two distributions (the first valley indicated by arrows in Figure 9). The binary segmentation can transform the very-low density resin in the void phase. The selection of different thresholds modifies the volume and shape of the binarized voids. An example of changes in the void features in correspondence of different thresholds for Type-A1 sample, is reported in Figure 10. The core of its

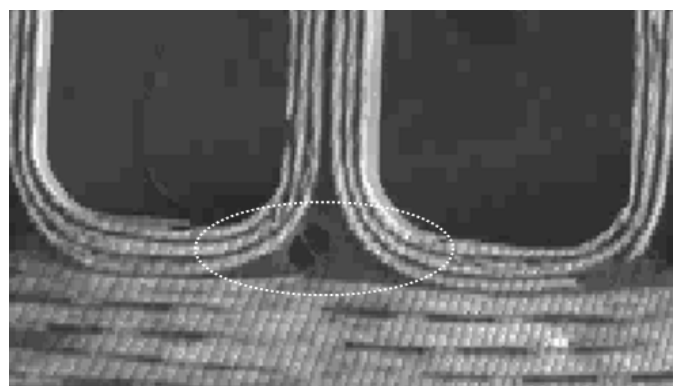
volume was segmented by selecting 50, 100, 150 luminosity threshold levels on the relevant histogram and the void distributions are reported in Figs, 10A, 10B and 10C, respectively.



A



B



C

**Figure 8.** Details of different defects relevant to Type-B2 sample: A) Tape deformation and distributed voids, B) High density material inclusions, C) Macro void between two conductors.

As can be seen, larger flat voids appear moving the threshold from 50 to 150 luminosity values. Figure 11 shows a magnified detail of a slice belonging to Type-A2 sample. Regions filled by the resin having different densities, are evident: higher close to the void borders, lower or completely

absent in the void center (see Figure 11A). The slice detail of Figure 11A is reported in Figures 11B and 11C after a segmentation performed selecting 150 and 50 luminosity thresholds, respectively. As visualized, virtual voids change their shape and size and the smaller ones disappear. Circle shadows in Figure 11A as well as in Figures 8B and 12B, are ring artifacts due to the non-linear behavior of detector' pixels.

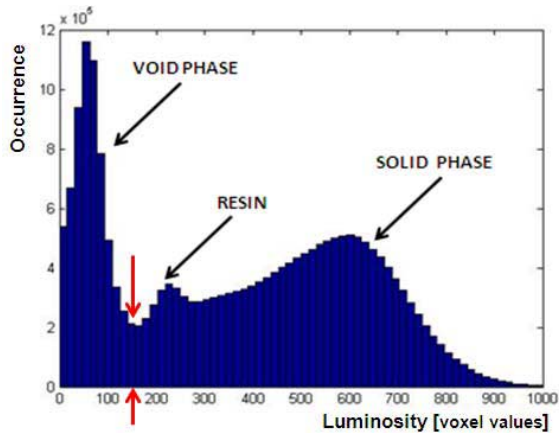


Figure 9. Example of luminosity histogram related to a coil sample.

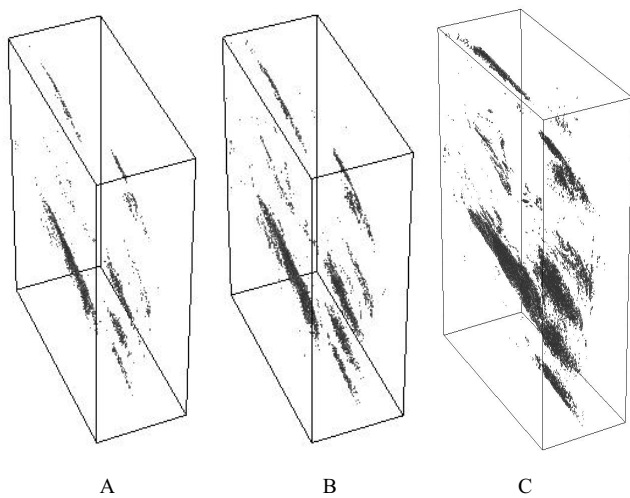


Figure 10. Binary segmentation of the Type-A1 sample reported in Figure 5 using different thresholds. A) 50, B) 100, C) 150 luminosity threshold-levels.

#### 4.2 BINARY SEGMENTATION FOR HIGH DENSITY PARTITIONS

The tomographic volumes of all the samples were binary segmented using higher luminosity threshold-levels to identify higher density inclusions such as anomalous mica-flakes or other solid inclusions. With reference to Figure 9, the selectect threshold was close to 1000. The result relevant to sample Type-B1 is reported in Figure 12 as an example. As can be seen in Figure 12A, some high density objects were discovered and some of them are indicated with arrows. The virtual volume has been successively sliced to verify if they are real defects or digital artifacts. Figure 12B reports the inclusion indicated in Figure 12A by the symbol (\*). As can be seen, the tape deformation suggests that this

inclusion is a real high density inclusion and not an image artifact. The same holds for the other high density inclusions.

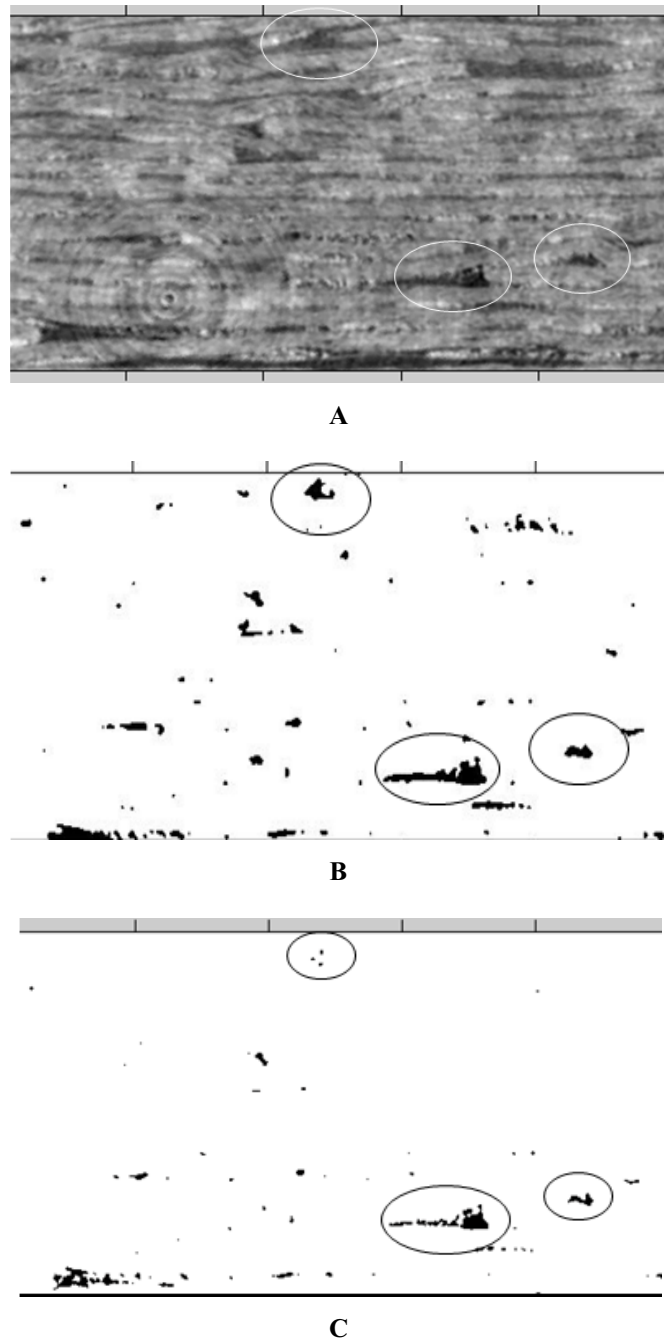
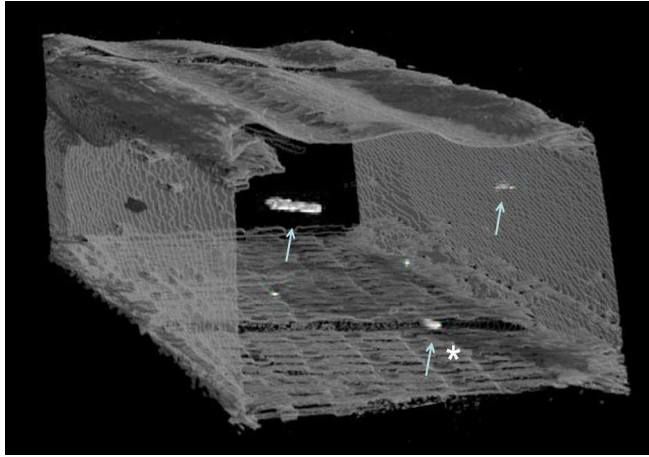


Figure 11. Detail of a slice relevant to sample Type-A2 of Figure 10, (A) and the relevant void distributions assuming 150 and 50 luminosity threshold level values.

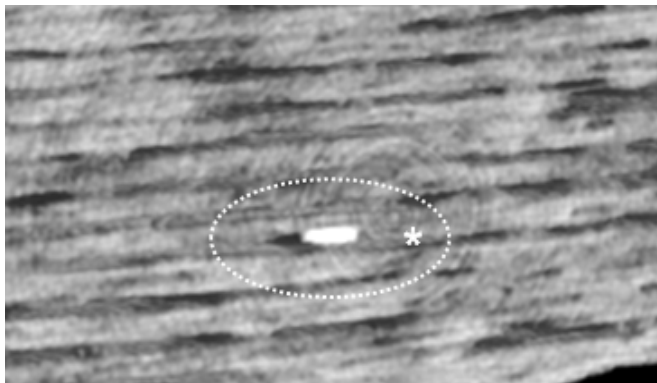
#### 4.3 MULTIPLE SEGMENTATION

The different solid phases inside the volumes (i.e., voids, resin and solid phase) can be distinguished resorting to the multi-segmentation that is partitioning the luminosity histogram in different intervals each one related to a specific phase. Here, the histogram of Figure 9 relevant to Type-B2 sample, has been segmented in three different phases that is, mica-tape plus fiber-glass, impregnation

resin and void enclosures with back-ground. The segmentation has been performed by selecting luminosity values close to the intersections of the luminosity distributions related to void-resin and resin-solid phases (close to 100 and 200 luminosity values, respectively) and Figure 13 shows the result.



A



B

**Figure 12.** Binary segmentation of Type-B1 sample. A) Distribution of the high density inclusions inside the volume and B) Sliced image of a specific (\*) inclusion.

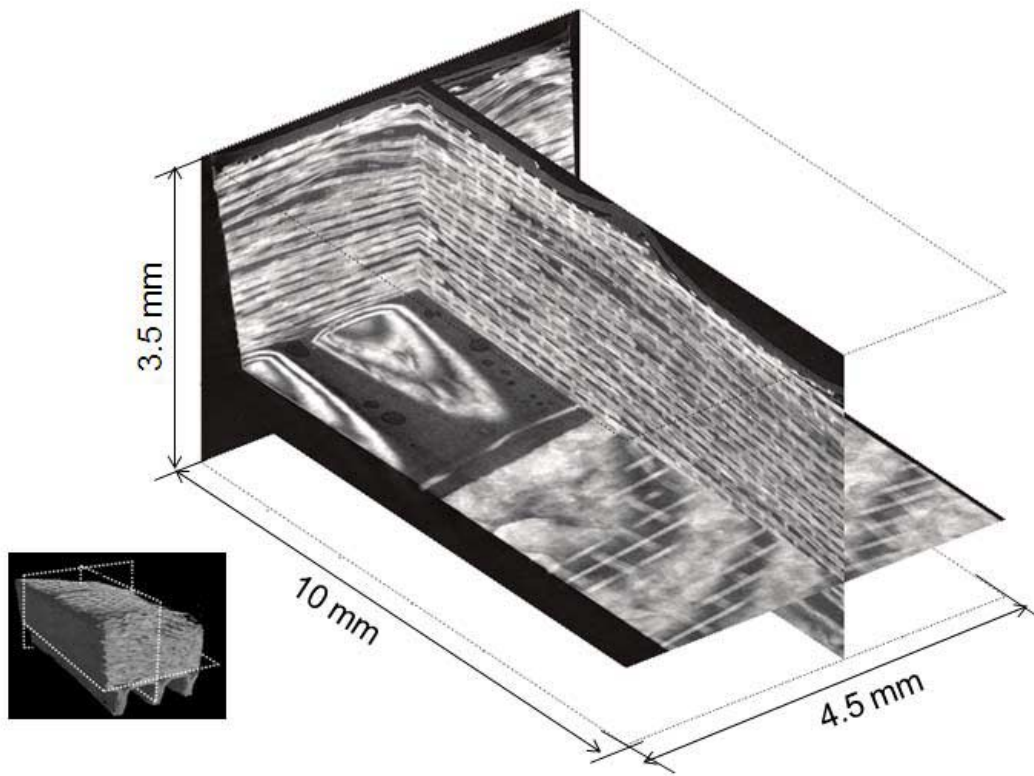
The 3D virtual volume has been sliced using three orthogonal planes considering the direction of the conductors as the main axis (Figure 13A) with the aim to improve the visualization of the details while Figure 13B reports the same sample after multiple segmentation. Sections have been evidenced on the 3D virtual volume and reported on both figures to facilitate their reading. As can be seen in Figure 13B, the lighter areas are relevant to the layers of mica-tape, included the turn insulation, and the fiber-glass (the large-texture of the fiber-glass is clearly identifiable). Both the void inclusions and the void space previously occupied by the conductors, are in black color while the impregnation resin is in light gray. This contrast evidences the position and the morphology of the void distribution inside the volume as darker spots. By using this technique, it is possible to observe the impregnation of both the turn insulation and the void space

between the conductors and the ground-wall insulation. It is well known that the presence of voids close to the corners of the conductors in a position where the electric field is intensified, can affect the reliability of the insulation system. Since some void inclusions were found in this position (see Figure 13B), a section of the 3D virtual volume that includes only the turn and the main insulation, close to the conductors, has been processed by applying the multi-segmentation procedure to only the sub-range of the luminosity histogram related to the void phase and the result is reported in Figure 14. As can be seen, the void-space previously occupied by the conductors is clearly visible in the figure as well as an interface composed by a distribution of voids or low-density resin. A rounded macro void has been also evidenced (indicated by an arrow in the figure). Once the different basic phases have been identified, the relevant relative permittivity can be assigned considering the voxel values as they appear after the multiple segmentation and the 3D electrostatic field distribution can be simulated in a realistic way on this basis, [10].

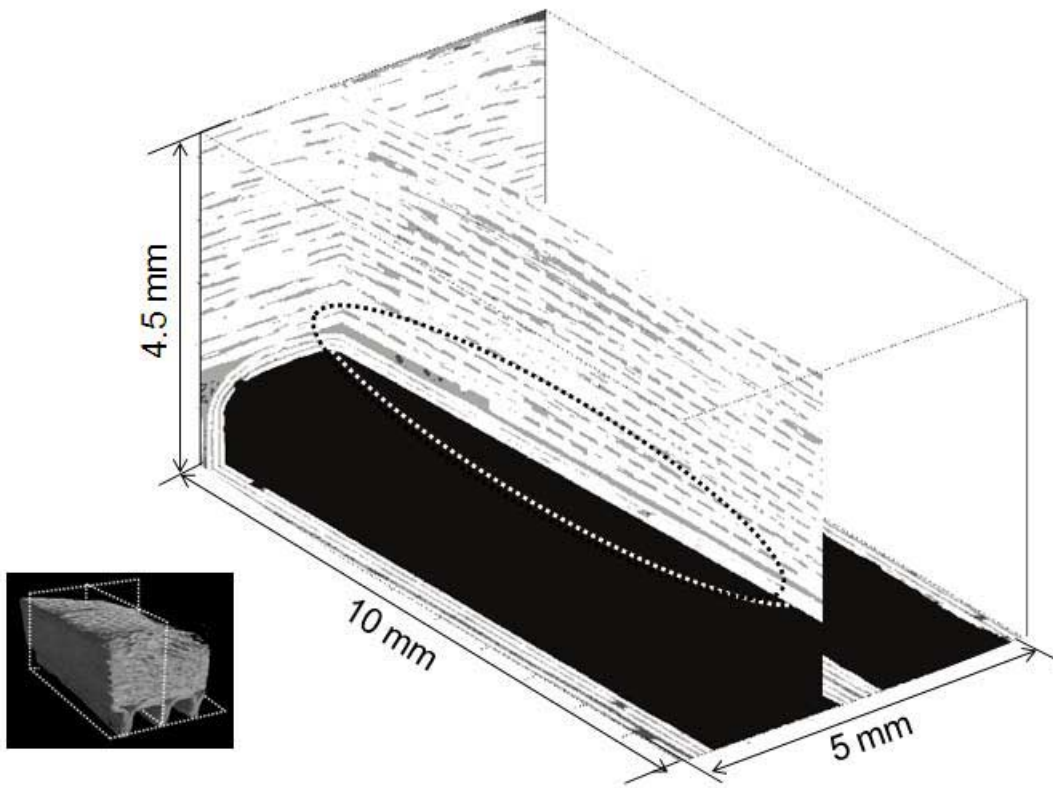
## 5 COMPARISON OF THE SAMPLES

The relationship between the insulation technology, the resin penetration and the void distribution within the volumes, has been evaluated resorting to a binary segmentation for void partition. Representative Volumes of Interest (VOI) of 5 mm x 5 mm x 2 mm were chosen far away from the sample edges of each 3D virtual images for a comparison. Figure 15 shows two VOIs relevant to Type-A2 (Figure 15A) and Type-B1 (Figure 15B) insulation. The threshold level for the binary segmentation has been fixed at about 100 normalized luminosity for both insulation typologies considering the image contrast between real voids and the low density impregnation resin. VOIs under test have been transformed in black and white 3D images accordingly.

Figures 16 and 17 show the VOIs relevant to samples Type-A1, -A2 (Figures 16A and 16B), and Type-B1, B2 (Figures 17A and 17B), respectively. It must be point out again that due to the problems related to the selection of threshold levels in partially overlapped gray-level distributions, voids as they appears in the segmented volumes, are a combination of real voids and low-density impregnation resin. Despite this approximation, the visual comparison of the void distributions allows significant considerations. Looking at Figure 16, flat and long voids (micro delaminations) characterize the two VOIs of Type-A insulation while more compact voids were found in both Type-B samples. It can be argued that both the thin-texture fiber-glass support and the polymeric films of the four-layer tape do not facilitate the resin penetration and generate these micro-delamination. Figure 18 shows a detail of a frontal slice of sample Type-A1. As can be seen by looking at the different gray-levels between the tape layers, it seems that the high density resin at the delamination edges prevents the complete filling of the flat void. On the contrary, the large fiber-glass texture of the two layer tape (Type-B) facilitates the resin penetration.



A



B

Figure 13. Sections of the tomographic volume of type B2 sample. A) before and B) after multiple segmentation.

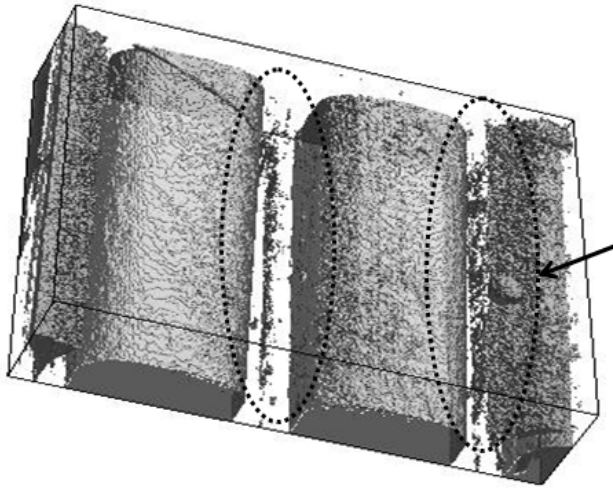


**Figure 14.** Detail of the void distribution relevant to the sample Type-B2 after a multi-phase segmentation.

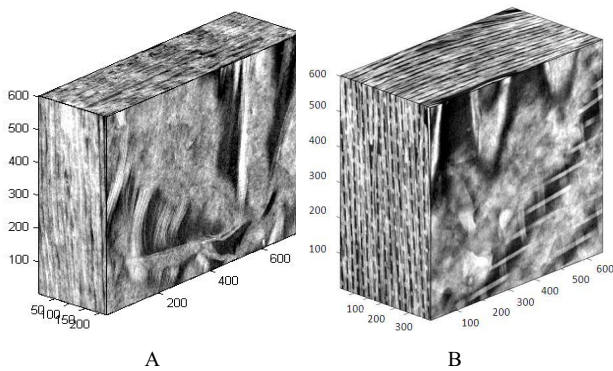


**Figure 15.** Examples of 3D digital images of VOIs relevant to A) Type-A2 and B) Type-B1 insulation.

A detail of a frontal slice of sample Type-B1 where the rounded voids are visible, is reported in Figure 19. Moreover, Type-B1 sample is characterized by less voids having smaller sizes with respect to B2 sample (Figure 20B).

## 6 CONCLUSIONS

The X-CT technique has been applied here to reconstruct, visualize and inspect in three dimensions, the internal features of two types of ground-wall insulation of ac rotating machines. The internal structure has been explored stacking tomographic slices and specialized image processing tools were used to visualize the inner structure as well as to discover the void distributions and the density anomalies of two types of insulation. It was found that the void distribution and the relevant morphological attributes are strictly connected with the tape characteristics and the VPI-process parameters. In particular, the thin fiber-glass texture and the presence of the polymeric films of the four-layer tapes tend to withstand to the resin penetration. The X-CT technology when applied to insulation having the same basic materials, can be used to select the best VPI parameters to minimize the void content below a satisfactory density.

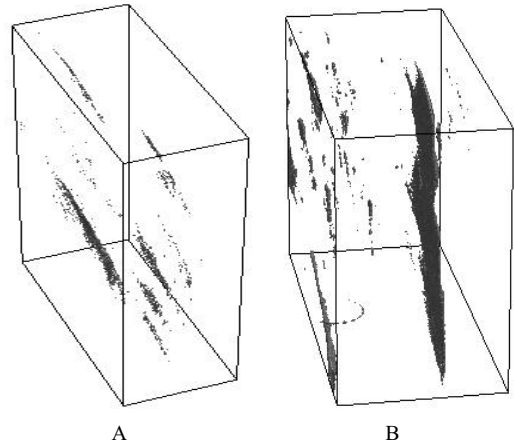


**Figure 16.** The segmented 3D digital image of a VOI relevant to insulation Type-A. A) Type-A1 and B) Type-A2 coil samples.

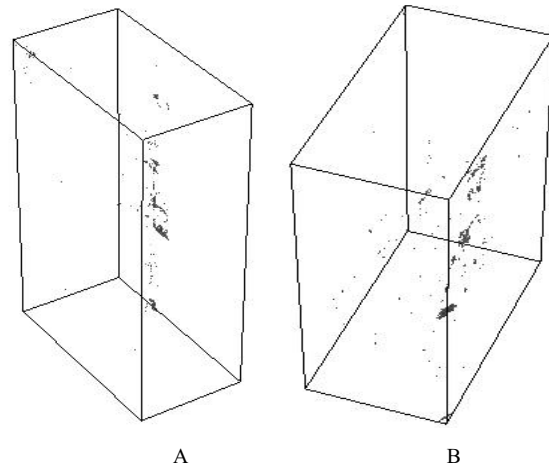


**Figure 17.** The segmented 3D digital image of a VOI relevant to insulation Type-B. A) Type-B1 and B) Type-B2 coil samples.

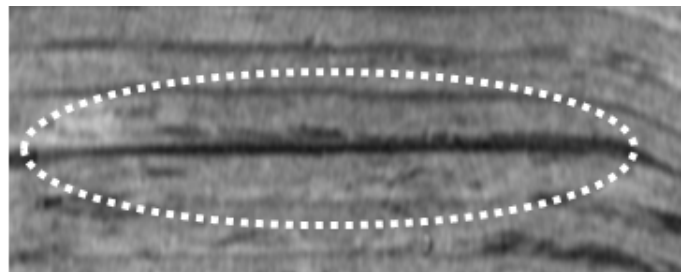


**Figure 18.** Detail of a tape delamination within Type-A1 sample.

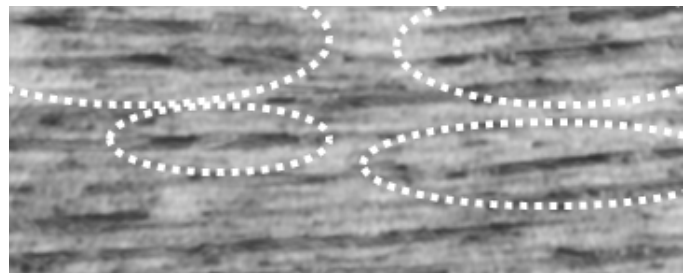


**Figure 19.** Detail of rounded voids within Type-B1 sample.

The application of X-CT technology to inspect the ground-wall insulation seems to be very promising when applied to compare the performances of different tape typologies, to analyze the resin penetration and the distribution of insulation anomalies. X-CT technology can open interesting perspectives in the quality certification of the VPI manufacturing process. Further investigations will be performed to discover how these density anomalies can affect the electric field distribution within the virtual volume and how these electric gradients can adversely affect the ageing progress, the breakdown mechanisms and partial discharges.

## ACKNOWLEDGEMENT

The financial support from “Università degli Studi di Trieste – Fondo Ricerca di Ateneo 2012”, is gratefully acknowledged.

## REFERENCES

- [1] G.C. Stone and G. Miller, “Progress in Rotating Machine Insulation Systems and Processing”, IEEE Electr. Insul. Mag., Vol. 29, No. 4, pp.45-51, 2013.
- [2] G.C. Stone and E.A. Boulter, I.Culbert, H.Dhirani, *Electrical Insulation for Rotating Machines*, John Wiley & Sons, USA, 2004.
- [3] R. Bruetsch, M. Tari, K. Froehlich, T. Weiers and R. Vogelsang, “Insulation Failure Mechanisms of Power Generators”, IEEE Electr. Insul. Magaz., Vol. 24, No. 4, pp. 17-25, 2008.
- [4] C. Hudon, M. Levesque, D.H. Nguyen, C. Millet and F. Truchon, “Root Cause Analysis of Generator Failures”, IEEE Int’l. Sympos. Electr. Insul., San Juan (Portorico), pp.199-203, 2012.
- [5] P. Marek, F. Senn, W. Grubelnik and W. Ladstatter, “Impact of New Motor and Generator Insulation Systems”, Enegeize On-Line (<http://eepublishers.co.za/article/energize-november-2007.html>), pp.51-55, 2007.
- [6] A.C. Kak, “*Principles of Computerized Tomographic Imaging*”, Soc. Industrial Appl. Mathematics (SIAM), Philadelphia, 2001.
- [7] J. Baruchel, J.Y. Buffiere, E. Maire, P. Merle and G. Peix, *X-Ray Tomography in Material Science*, Hermes Science Publication, Paris, France, 2000.
- [8] L. De Chiffre, S. Carmignato, J.P. Kruth, R. Schmitt and A. Weckenmann, “Industrial Applications of Computed Tomography”, Annals of Int’l. Accademy for Production Engineering – Manufacturing Technology, Vol. 63, pp. 655-677, 2014.
- [9] L. Salvo, P. Cloetens, E. Maire, S. Zabler, J.J. Blandin, J.Y. Buffière, W. Ludwig, E. Boller, D. Bellet and C. Jossierond: “X-Ray Micro-Tomography: An Attractive Characterization Technique in Materials Science”, Nuclear Instrum. and Methods in Physics Research, Section B: Beam Interactions with Materials and Atoms, Vol. 200, pp. 273-286, 2003.

- [10] M. Piller, G. Schena, A. Contin and G. Rabach, “Ground-Wall Insulation System Analysis Combining Advanced Imaging Techniques and Numerical Simulation”, J. Electric Power Systems Research, Ed. Elsevier Publishing, Vol. 116, pp. 444-450, 2014.
- [11] M. Piller, D. Casagrande, G. Schena and M. Santini, “Pore-scale simulation of laminar flow through porous media”, J. Phys.: Conf. Series (JPCS), pp.153-162, 2014.
- [12] M. Piller, G. Schena, M. Nolich, S. Favretto, F. Radaelli and E. Rossi, “Analysis of hydraulic permeability in porous media: from high resolution X-ray tomography to direct numerical simulation”, Transport in Porus Media, Vol. 80, No. 1, pp. 7-78, 2009.
- [13] J. Radon and P. Parks, “On the Determination of Functions from their Integral Values along Certain manifolds”, IEEE Trans. Med. Imag., Vol. 5, pp. 170-176, 1986.
- [14] L.A. Feldkamp, L.C. Davis and J.W. Kress, “Practical Cone-Beam Algorithm”, J. Opt. Soc. Am., Vol.1, pp.612-619, 1984.
- [15] S.K. Mitra and G. Sicuranza, *Nonlinear Image Processing*, Academic Press, Ch. 2, 2001.
- [16] N. Otsu, “A Threshold Selection Method from Grey-Level Histograms”, IEEE Trans. Systems Man Cybernetics”, Vol. 9, pp. 62-66 (1979).



**Gianni Schena** received his Ph.D. degree in engineering from the Imperial College of London, UK, in 1994. He is currently an associate professor of the Department of Engineering and Architecture of the University of Trieste, Italy. His research interest includes high resolution X-ray tomography, image analysis of reservoir rocks, numerical simulation of two-phase flow through porous media.



**Alfredo Contin** (M’87) is currently an associate professor at the Department of Engineering and Architecture of the University of Trieste, Italy. His fields of interest are characterization, aging and diagnostics of insulation materials and systems by means of partial discharges.



**Marzio Piller** received his Ph.D. degree in mechanical engineering from the University of Trieste, Italy, in 2002. He is currently a research assistant of the Department of Engineering and Architecture of the same University. His research interest includes numerical simulation of turbulence and flow through porous media, analytical solution of laminar heat convection and numerical simulation of geothermal flows.